Electronic Supplementary Information (ESI)

Supplementary Information

Asymmetric Evaporation for Efficient and Simultaneous Extraction of Freshwater, Salt, and Electrical Energy from Seawater

Yitian Wu,[a] Chaoliang Ma,[a] Kangxin Zhu,[a] Lizheng Jin,[a] Lvfu Song,[a] Lanze Li,[a]

Yingzhuo Lu,[a] Yu Zheng,[a] Yaoxin Zhang,[bc] Xin Zheng,[a] Sai Wu,[a] Yajun Pang,[*a]

Zhehong Shen,[a] Swee Ching Tan,[*b] and Hao Chen[*a]

[a] College of Chemistry and Materials Engineering, Zhejiang Provincial Collaborative Innovation Center for Bamboo Resources and High-Efficiency Utilization, National Engineering and Technology Research Center of Wood-based Resources Comprehensive Utilization, Key Laboratory of Wood Science and Technology of Zhejiang Province, Zhejiang A&F University, Hangzhou 311300, P.R. China.

[b] Department of Materials Science and Engineering, National University of Singapore, 9 Engineering drive 1, Singapore 117575.

[c] China-UK Low Carbon College, Shanghai Jiao Tong University, Shanghai 201036, P.R. China.

* yjpang@zafu.edu.cn (Y. Pang);
* msetansc@nus.edu.sg (S.C. Tan);
* haochen@zafu.edu.cn (H. Chen)

Table of contents:

Supplementary Materials and Methods

1. The calculation of the solar-to-vapor efficiency

In order to calculate the efficiency of solar evaporator under irradiation, the water evaporation rate in dark environment was measured using a 3.5 wt% NaCl solution (simulated seawater). The energy efficiency (η) for solar-to-vapor conversion can be calculated using the following equation:[1, 2]

$$\eta = m \times (H_{LV} + W_{least}) / Q_i \tag{1}$$

In this equation, m represents the measured water evaporation rate generated by the solar evaporator (kg m^{-2} h^{-1}), which is the total water evaporation under a certain intensity of light minus the natural evaporation in dark environment. Q_i denotes the solar light intensity reaching the device every hour (kW m^{-2} h^{-1}). H_{LV} is the overall enthalpy change of the liquid-vapor phase transition (2,257 kJ kg^{-1}). W_{least} is the theoretical least work required to separate the salt solution into solid salts and pure water. According to the literature,[3] it has been reported that the energy consumption for separating a 3.5 wt% NaCl solution into pure water and solid salt is approximately 10.75 kJ kg^{-1}. This value is equivalent to an energy consumption of approximately 10.39 kJ kg^{-1} when separating it solely into pure water. We used this approximate value for our calculations.

2. Measurement of salt concentration distribution on PAM-CBF disc in AEE

To determine the distribution of salt concentration on the PAM-CBF disc within the AEE, the following experimental procedure was employed. First, the PAM-CBF disc was immersed in seawater, and its weight was recorded at 30-minute intervals until a stable weight was achieved. This step was conducted prior to assembling the disc into the AEE. After the assembly process, the PAM-CBF disc was exposed to sunlight for a period of 10 hours. Subsequently, the disc was cut into 48 pieces. Following the

cutting process, digital photographs of all the PAM-CBF slices were captured and the area of each slice was calculated using ImageJ software. Next, the samples were immersed in 12 mL of deionized water and treated with intermittent sonication for over 2 days. The salt concentration of the leachate was measured using a conductivity meter (AZ 86505). Finally, the mass fraction of salt (ω) was calculated using the following equation:

$$\omega = (C \times V) \times A_0 / (A \times m_2 - A \times m_1) \tag{2}$$

In this equation, C represents the NaCl concentration of the leachate, V denotes the volume of the leachate, A signifies the area of the sample, A_0 represents the area of the cut sample fragments, and m_1 and m_2 refer to the weight of the PAM-CBF disc before and after seawater absorption, respectively.

Supplementary Note 1: Computational Fluid Dynamics Simulation

Model description

The model simulates two phases: seawater (l) and water vapor (v), with seawater comprising salt (cl) and water. Mass transfer takes place between the seawater and water vapor, and salt diffusion occurs within the seawater phase. The simulation uses laminar flow to account for the low Reynolds number throughout the process.

Conservation equations of the current 2-phase model:

Mass conservation:

$$\frac{\partial}{\partial t}\left(f_l\rho_l\right) + \nabla \times \left(f_l\rho_l\vec{u_l}\right) = -M_{lv}$$

(3)

$$\frac{\partial}{\partial t}\left(f_v\rho_v\right) = M_{lv}$$

(4)

Where M_{lv} is the mass source due to water evaporation, f_l, ρ_l, and u_l represent the volume fraction, density, and velocity of seawater, respectively, and similarly, f_v, ρ_v, and u_v refer to the volume fraction, density, and velocity of water vapor.

Momentum conservations:

$$\frac{\partial}{\partial t}\left(f_l\rho_l\vec{u_l}\right) + \nabla \times \left(f_l\rho_l\vec{u_l} \otimes \vec{u_l}\right) = -f_l\nabla P + \nabla \cdot \overline{\overline{\tau}}_l + \vec{F}$$

(5)

Where P represents the pressure, $\overline{\overline{\tau}}_l$ is the stress tensor, and $\vec{F}$ represents the momentum sources due to body forces.

Species conservations:

The general transport equation for solute transport through a system under advection-diffusion is commonly expressed as follows:

$$\frac{\partial}{\partial t}\left(f_l\rho_l c_l\right) + \nabla \times \left(f_l\rho_l\vec{u_l}c_l\right) = \nabla \times (f_l\rho_l D_l\nabla c_l) - C_{lv}$$

(6)

Where c represents the concentration of the solute, D denotes the diffusion coefficient, with a value of 1.5×10^{-9} m^2 s^{-4}, $\vec{v}$ represents the velocity of the fluid, c_l is the concentration (wt%) of the seawater, and C_{lv} signifies the source term attributed to generation or dissipation.

Calculation of the characteristic length of the PAM-CBF disc

The characteristic length of the PAM-CBF disc was obtained by measuring the diameters of 50 fibers in the SEM image and calculating the average.

Calculation of the porosity of the PAM-CBF disc

The porosity of the PAM-CBF disc was determined by measuring the water absorption of the disc. The porosity (p) can be calculated using the following formula:

$$p = [(m_{wet} - m_{dry}) / \rho_{water}] / [m_{dry} / \rho_{sample} + (m_{wet} - m_{dry}) / \rho_{water}] \qquad (7)$$

Where m_{dry} and m_{wet} are the weight of PAM-CBF disc before and after wetting, ρ_{sample} and ρ_{water} are the density of PAM-CBF disc and water, respectively.

Calculation of the average water content in the PAM-CBF disc

First, water content distribution results were obtained by CFD simulation. Subsequently, the number of pixels (indicative of specific water content levels) within each region of the simulation results was counted using appropriate image processing software, such as Photoshop. The formula for calculating the average water content is as follows:

$$C_{average} = (C_1 \times N_1 + C_2 \times N_2 + ... + C_n \times N_n) / (N_1 + N_2 + ... + N_n) \qquad (8)$$

Where $C_{average}$ is the average water content, C_1 to C_n are the water contents of the different areas, and N_1 to N_n are the pixel numbers of the different areas.

Parameters of the simulation

See details in Table S3.

Supplementary Tables (Table S1 to S5)

Table S1. Cost calculation of the AEE system.

Materials	Price ($ g^{-1})	Dosage (g m^{-2})	Cost ($ m^{-2})
Bamboo fiber	4.63×10^{-4}	2300.1	1.06
Acrylamide (AM)	9.26×10^{-4}	1150.0	1.06
N,N'-Methylenebis (acrylamide) (MBA)	4.01×10^{-3}	115.0	0.46
Potassium persulfate (K$_2$S$_2$O$_8$)	6.17×10^{-4}	11.5	0.007
Total Price	/	/	2.59

The quantities of bamboo fiber, AM, MBA, and K$_2$S$_2$O$_8$ used in the PAM-CBF disc were 334.2, 436.7, 43.67, and 4.37 g m^{-2}, respectively. Hence, **the cost of producing the PAM-CBF disc amounted to 0.73 $ m^{-2}.**

For the PAM-BF column, the amounts of bamboo fiber, AM, MBA, and K$_2$S$_2$O$_8$ utilized were 1965.87, 713.0, 71.30, and 7.13 g m^{-2}, respectively. Consequently, **the cost of manufacturing the PAM-BF column equated to 1.86 $ m^{-2}.**

Table S2. Cost comparison between AEE and other evaporators.

Reference	Cost of the photothermal material ($ m^{-2})	Cost of the evaporator ($ m^{-2})
Ref. 4[4]	/	3
Ref. 5[5]	/	2.75
Ref. 6[6]	< 10	/
Ref. 7[7]	/	250
Ref. 8[8]	/	14.65
Ref. 9[9]	/	2.4
Ref. 10[10]	0.78	/
Ref. 11[11]	/	39
Ref. 12[12]	/	6
Ref. 13[13]	/	14.9
This work	**0.73**	**2.59**

Table S3. Parameters for CFD simulation.

Simulation parameters	Experimental data
The radius of PAM-CBF disc	18 mm
The thickness of PAM-CBF disc	1.74 mm
The radius of PAM-BF stalk	13 mm
Dry mass of PAM-CBF disc	0.2510 g
The quality of absorbed salt water	1.5353 g
Contact angle (water)	0°
Characteristic length	33.34 μm
Density	0.937 g cm^{-3}
Porosity	0.865
Initial water (salt) mass fraction	96.5 wt% (3.5 wt%)
Pressure at the inlet	0
Salt diffusion coefficient	1.5×10^{-9} m^2 s^{-1}
Salt density	2000 kg m^{-3}
Salt dynamic viscosity	1 Pa s
Water density	997 kg m^{-3}
Water dynamic viscosity	8.9×10^{-4} Pa s
Analysis type	Transient, double precision
Time step	1 s
Residual target	1×10^{-8}
Max interactions per loop	20
Total time	1000 s, 50000 s

Table S4. Evaporation rates and solar-to-vapor efficiencies of our SEE, our AEE, and other reported SEEs based on different materials.

Materials of evaporators	Evaporation rate (kg m^{-2} h^{-1})	Solar-to-vapor efficiency (%)
Polyelectrolyte hydrogel foam, Adv. Energy Mater. (2019)[14]	1.3	79
Small molecule modified polyurethane foam, Adv. Mater. (2020)[15]	1.27	87.2
Polydimethylsiloxane sponge coated with carbon nanotubes, Adv. Energy Mater. (2019)[16]	1.35	87.4
MXene and graphene oxide-coated polystyrene, Adv. Energy Mater. (2019)[17]	1.37	90.1
Polydopamine-coated cellulose membrane, Sci. Adv. (2020)[18]	1.53	88.6
Carbon nanotube-embedded filter paper discs, Energy Environ. Sci. (2019)[2]	1.42	81.2
Janus carbon nanotubes, Sci. Adv. (2024)[19]	1.47	~80
Bio-graphene coated sponge, Nat.Water (2023)[20]	1.42	89.4
This work (SEE)	**1.65**	**85.8**
This work (AEE)	**1.79**	**94.4**
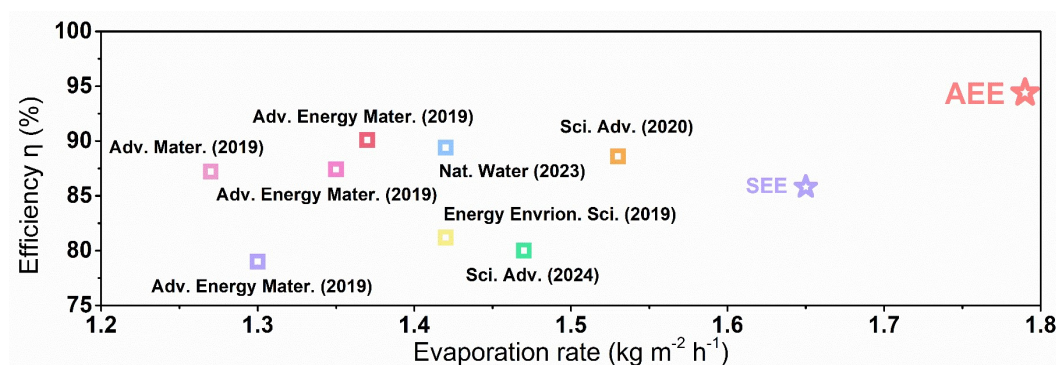
Table S5. Comparison of salt collection performance between our AEE-based device and previous devices using evaporators.

Materials of evaporators	Salt collection rate (g m^{-2} h^{-1})	Operation time (h)
Nylon 66/carbon black nanofiber film, Sol. RRL (2022)[21]	55	9
Printed air-laid paper, Desalination (2020)[22]	25	12
Functionalized polyacrylonitrile textile, Chem. Eng. J. (2021)[23]	20	60
MOFs-based nanorod arrays, Desalination (2022)[24]	47	120
Carbon nanotube-embedded filter paper discs, Energy Environ. Sci. (2019)[2]	37	630
3D nitrocellulose membrane, Environ. Sci. Technol. (2023)[25]	97 (using 10 wt% brine)	240
Nano/micro-structured titania layer on titanium mesh, Nat. Commun. (2024)[26]	44.7	96
This work (AEE)	**40**	**1800**

Table S6. Comparison of output voltages for our device based on AEE and previous devices utilizing evaporators.

Materials of evaporators	Test conditon	Core materials used for electrical energy output	Voltage (mV)
Polydimethylsiloxane sponge coated with carbon nanotubes, Adv. Energy Mater. (2019)[16]	One-sun	Thermoelectric module	55
Starch–polyacrylamide hydrogel, Energy Environ. Sci. (2022)[27]	One-sun	Thermoelectric module	105
Carbon nanotube film, Energy Environ. Sci. (2017)[28]	One-sun	Ion-exchange membrane	62
Multi-layered bionic light-trapping membrane, Nat. Commun. (2022)[29]	One-sun	Evaporation-driven ion flow (decorated porous membrane)	275
Carbon nanotube-conducting polymer sponge, Nano Energy (2022)[30]	One-sun	Evaporation-driven ion flow (ion-selective channels)	117.8
Bio-graphene coated sponge (2023)[20]	One-sun	Ion-exchange membrane	220
Living lotus leaf, Nat. Water (2024)[31]	/	Evaporation-driven ion flow	250
This work (PAM-CBF disc)	One-sun	Evaporation-driven ion flow **(Positively charged PAM hydrogel)**	**350**
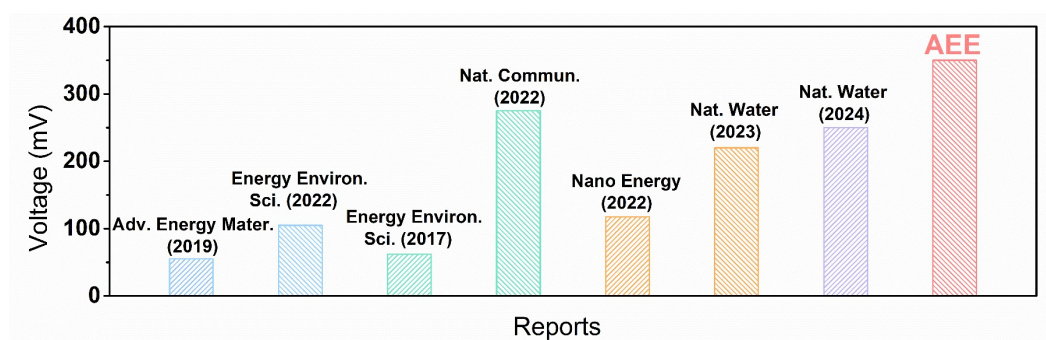
Supplementary Figures (Fig. S1 to S33)
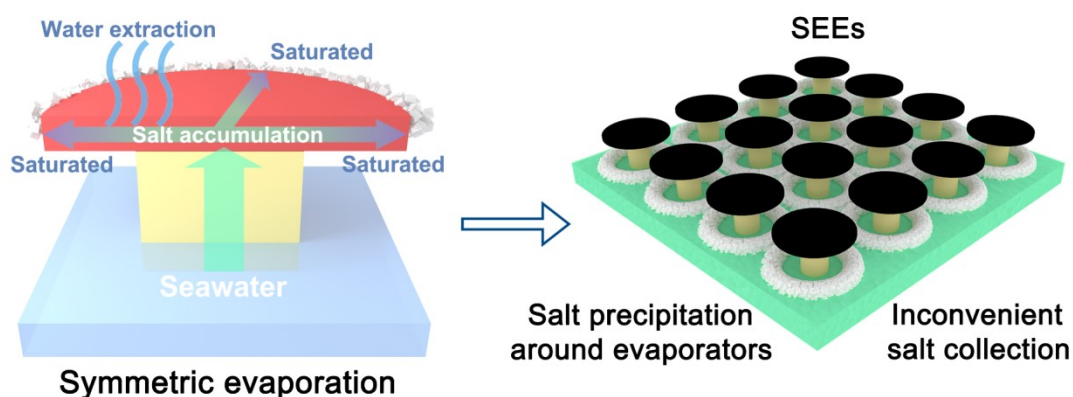
Fig. S1. Schematic illustration of symmetric evaporation resulting in the dispersion of salt collection.

In traditional evaporators, water is evaporated in a symmetric manner. This type of evaporation is known as symmetric evaporation, and the evaporators that operate in this mode are referred to as symmetric evaporation evaporators (SEEs), as illustrated in Fig. S1. With symmetric evaporation, water transport and salt accumulation also occur symmetrically within the SEE. This implies that the ratio of seawater supply to evaporation loss on the evaporation surface remains symmetrical across different regions, and the solid salts formed during evaporation are evenly distributed on the SEE.

In practical applications, it is often necessary to arrange multiple evaporators in arrays to achieve large-scale water and salt acquisition. **In such cases, the salt produced by the SEEs will be dispersed over a larger area, which significantly increases the difficulties associated with salt collection. Consequently, SEEs are not conducive to efficient solid salt collection.**
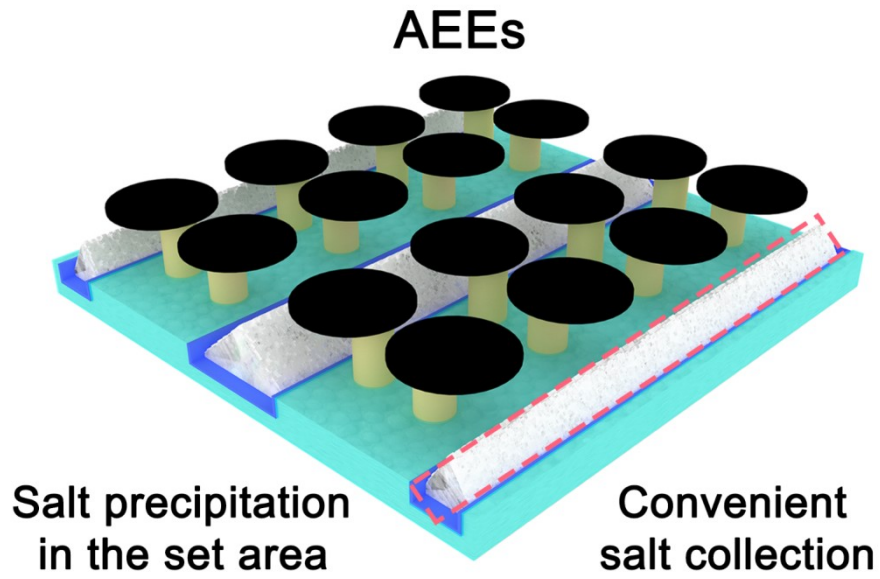
Fig. S2. Schematic illustration of efficient salt collection by AEEs.

In contrast to the SEE, the AEE controls the precipitation of salt in a designed area. As a result, solid salt accumulates and falls by gravity, collecting in a concentrated area. This significantly improves the ease of salt collection.
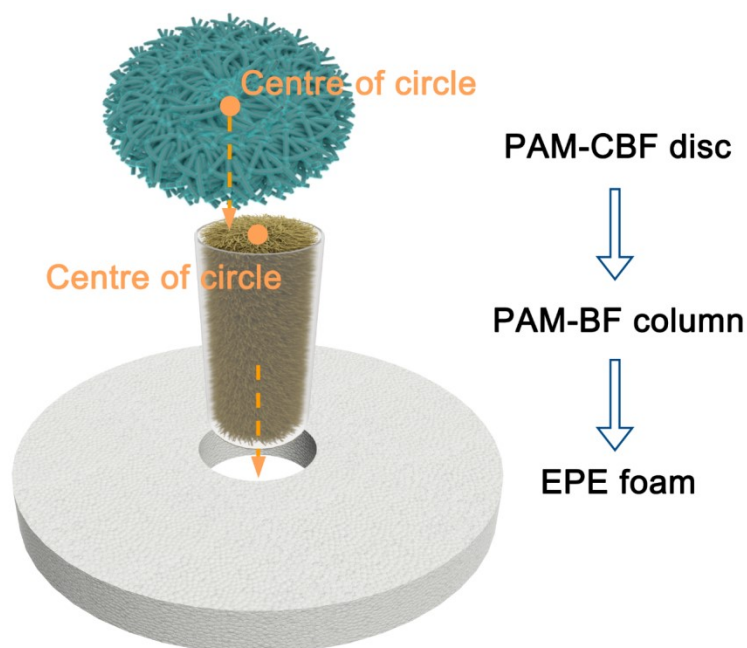
Fig. S3. Schematic illustration of the assembly of evaporators including SEE, AEE, and AEE (100% offset).

The evaporators, including SEE, AEE, and AEE (100% offset), consist of three main components: the PAM-CBF disc as the photothermal component, the PAM-BF column as the water transport component, and commercial EPE foam as the insulation component. The overall structure of these evaporators is identical, as depicted in Fig. S3. **The only distinction lies in the distance between the centers of the PAM-CBF disc and the PAM-BF column, which is 0 cm in SEE, 0.3 cm in AEE, and 0.6 cm in AEE (100% offset).**
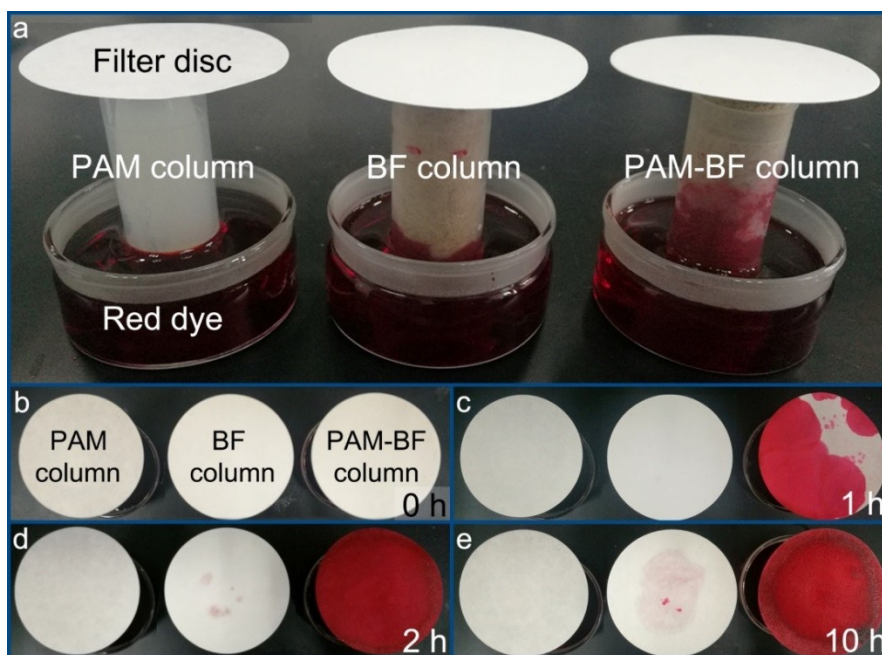
Fig. S4. Comparison of water delivery ability of PAM column, BF column, and PAM-BF column. (a) Experimental setup used to test water delivery capacity. (b-e) Sequential images showing red dye diffusion through different water transport columns from the bottom container to the top filter paper disc at different time intervals (0, 1, 2, and 10 hours).

To demonstrate the superior performance of the PAM-BF column, a custom water delivery velocity test setup was constructed using containers filled with red dye solution, different water delivery columns, and filter paper discs, as depicted in Fig. S4. The water delivery velocity of the columns was determined by observing the diffusion of the red dye solution over time on the filter paper discs. The results indicate that **the PAM-BF column owns exceptional water transfer capacity.** This can be attributed to the capillary structure within the bamboo fibers and the excellent wettability of the PAM hydrogel, where the capillary structure promotes efficient water transport and the PAM hydrogel effectively connects the bamboo fibers.
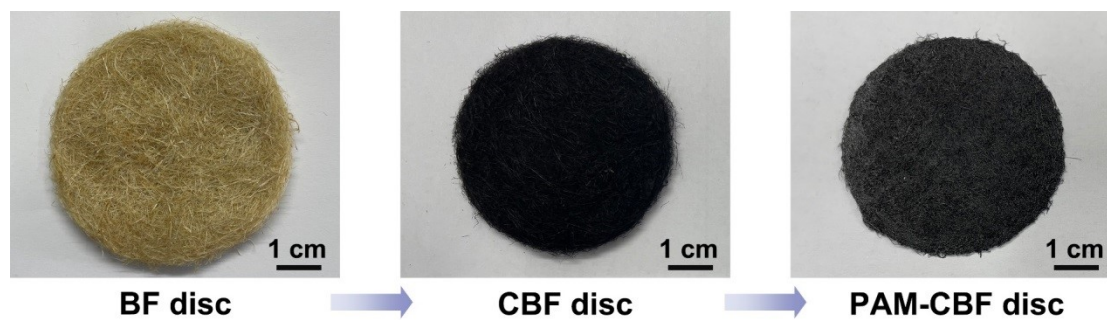
Fig. S5. Images of BF disc, CBF disc, and PAM-CBF disc.

After the carbonization process, the color of the BF disc changes from yellow to black, indicating an improvement in its light absorption capacity. Moreover, the PAM-CBF disc maintains its black color even after the in-situ polymerization of PAM.
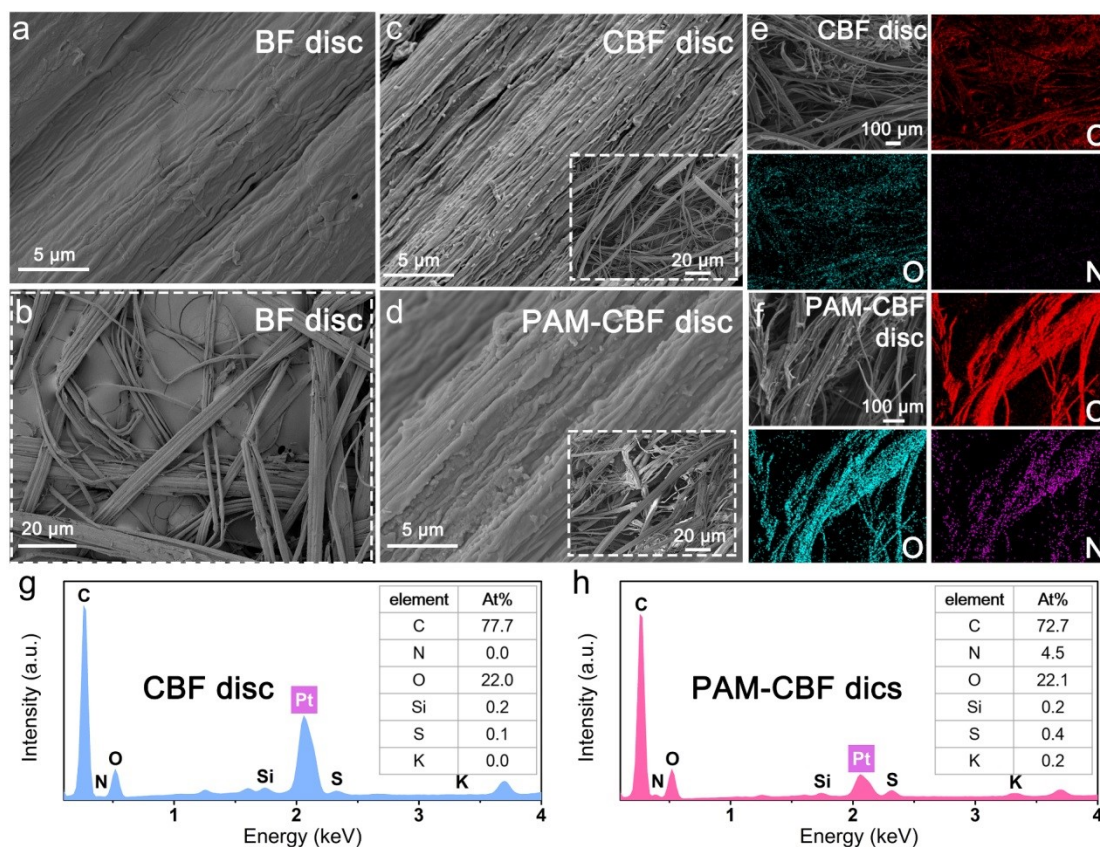
Fig. S6. SEM characterization of BF disc, CBF disc, and PAM-CBF disc. SEM images of (a, b) BF disc, (c) CBF disc, and (d) PAM-CBF disc. SEM elemental mapping images of (e) CBF disc and (f) PAM-CBF disc. EDS spectra of (g) CBF disc and (h) PAM-CBF disc.

The presence of additional nitrogen in the PAM-CBF disc compared to the CBF disc indicates the successful modification of PAM on the surface of CBF.
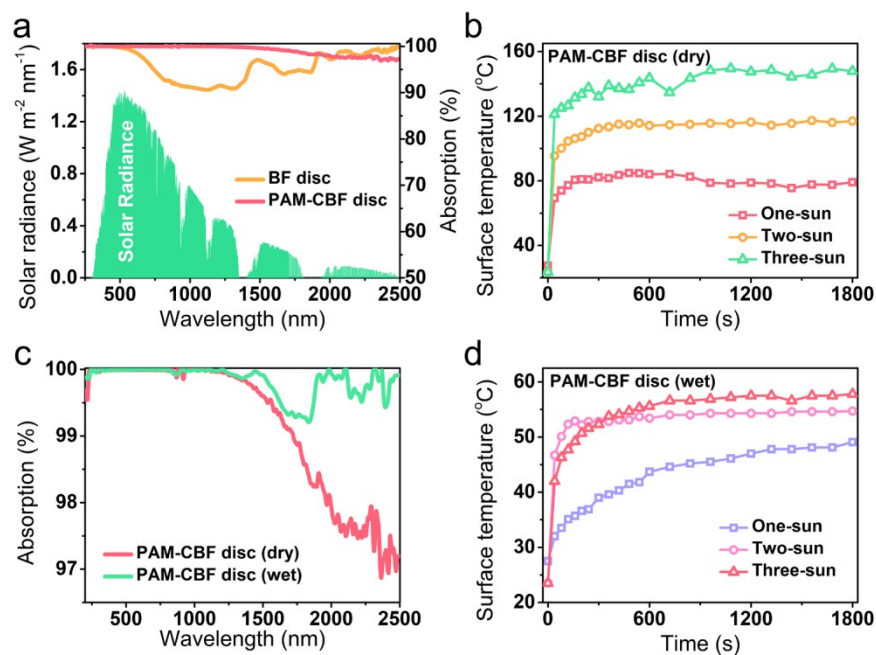
Fig. S7. Light absorption and photo-thermal conversion performance of PAM-CBF disc. (a) UV-Vis-near-infrared spectra of BF disc (orange) and PAM-CBF disc (red). The green curve represents the normalized spectral solar irradiance density of the air mass 1.5 global (AM 1.5) tilt solar spectrum. (b) Temperature variation profiles of PAM-CBF disc in a dry state under irradiation with different intensities. (c) UV-Vis-near-infrared spectra of PAM-CBF disc in the dry state (red) and wet state (during evaporation) (green). (d) Temperature variation profiles of PAM-CBF disc in wet state under irradiation with different intensities.

After undergoing carbonization and in-situ polymerization processes, **the PAM-CBF disc exhibits a significant improvement in light absorption performance compared to the BF disc**. This improvement is observed in both dry and wet states, showcasing exceptional light absorption capabilities and photothermal performance. The reason for the enhanced light absorption performance of wet PAM-CBF discs compared to dry PAM-CBF discs is that when PAM absorbs water, it undergoes a

transformation from a white appearance to a transparent state. This change in optical properties leads to a decrease in reflectivity, resulting in enhanced light absorption.
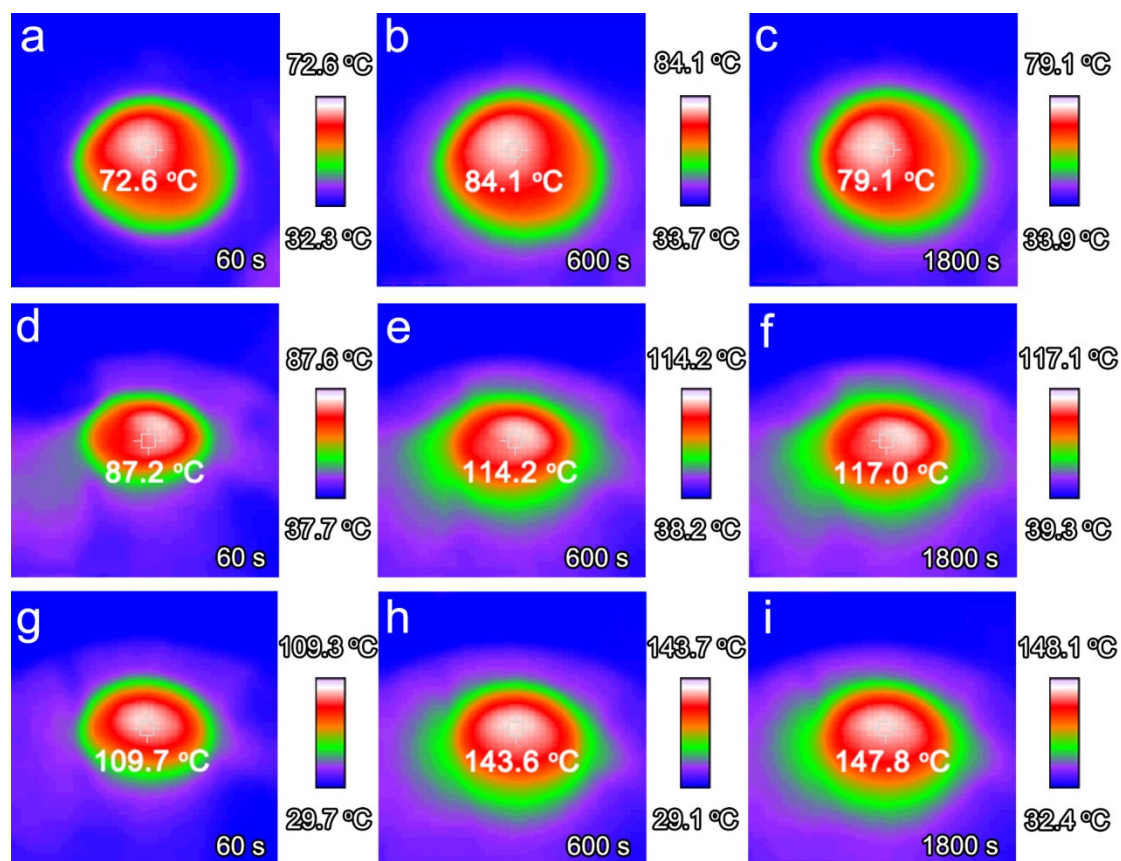
Fig. S8. Infrared images of the dry PAM-CBF disc under different irradiation conditions: (a-c) one-sun irradiation; (d-f) two-sun irradiation; and (g-i) three-sun irradiation.

Under different intensities of irradiation, the temperature of the PAM-CBF disc (in its dry state) rapidly increases at the beginning. Subsequently, it consistently maintains high and stable temperatures after a certain period of irradiation. These results provide strong evidence for the exceptional photothermal performance demonstrated by the PAM-CBF disc.
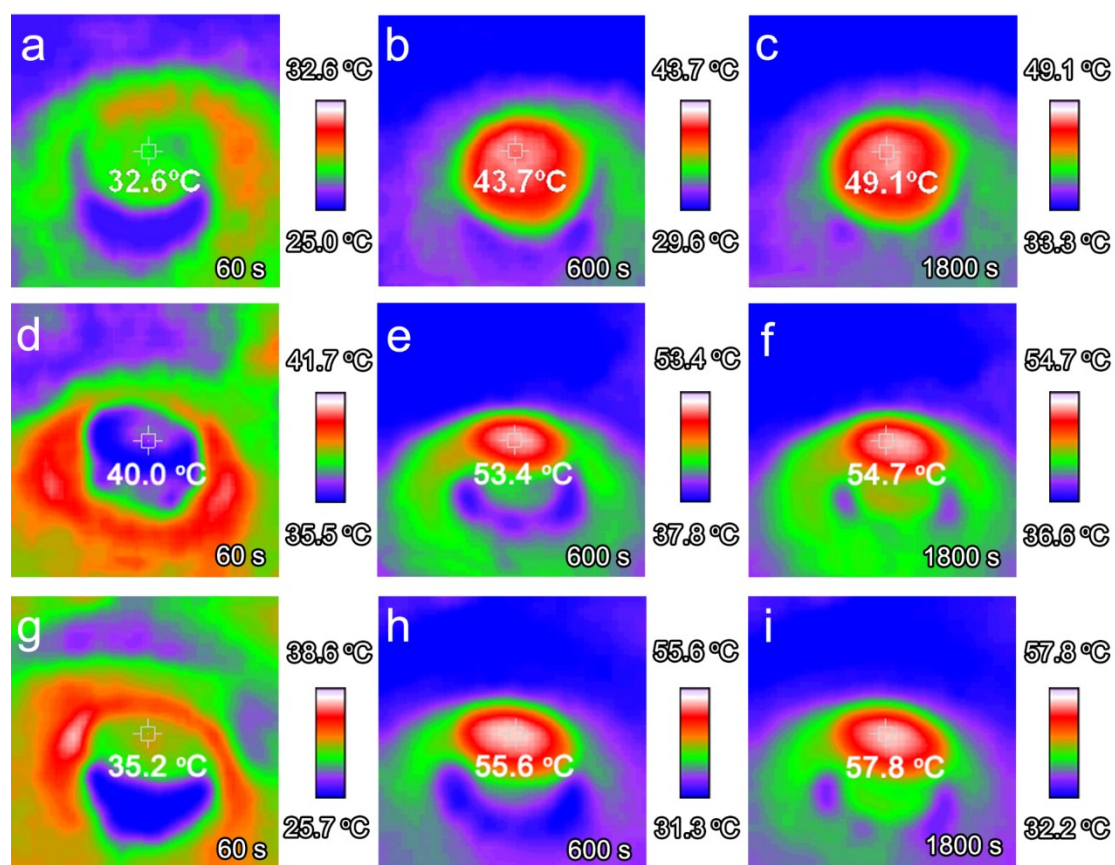
Fig. S9. Infrared images of the wet PAM-CBF disc under different irradiation conditions: (a-c) one-sun irradiation; (d-f) two-sun irradiation; and (g-i) three-sun irradiation.

Under varying intensities of irradiation, the initial and stable temperatures of wet PAM-CBF disc are lower compared to the dry PAM-CBF disc. This discrepancy can be attributed to the consumption of thermal energy by water evaporation in the wet state during photothermal conversion. Nonetheless, the wet PAM-CBF disc can maintain a high and stable temperature after a period of irradiation.
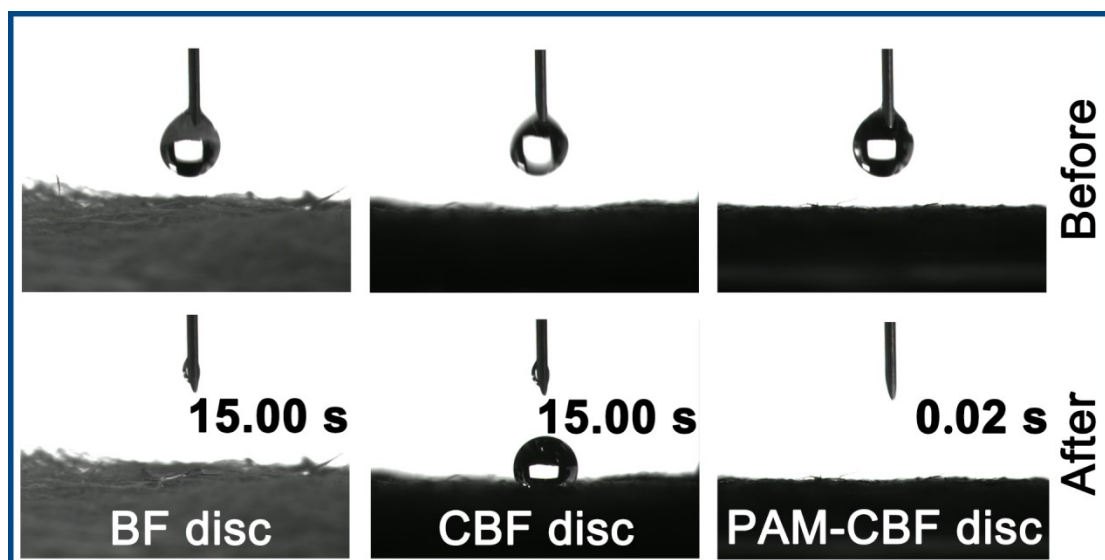
Fig. S10. Comparison of wettability of the BF disc, CBF disc, and PAM-CBF disc. The images depict a water drop suspended above the discs and the moment after it makes contact with the surface of each disc.

The absorption of a water droplet on the surface of the PAM-CBF disc, as demonstrated in Fig. S10, occurs within a remarkably brief period of 0.02 seconds. In contrast, the process takes a notably longer duration of 15.00 seconds on the surface of BF disc. Additionally, a water droplet placed on the CBF disc remains unabsorbed even after 15.00 seconds. **This experiment highlights the exceptional wettability of the PAM-CBF disc, indicating its potential as a highly promising candidate for solar evaporation applications.**
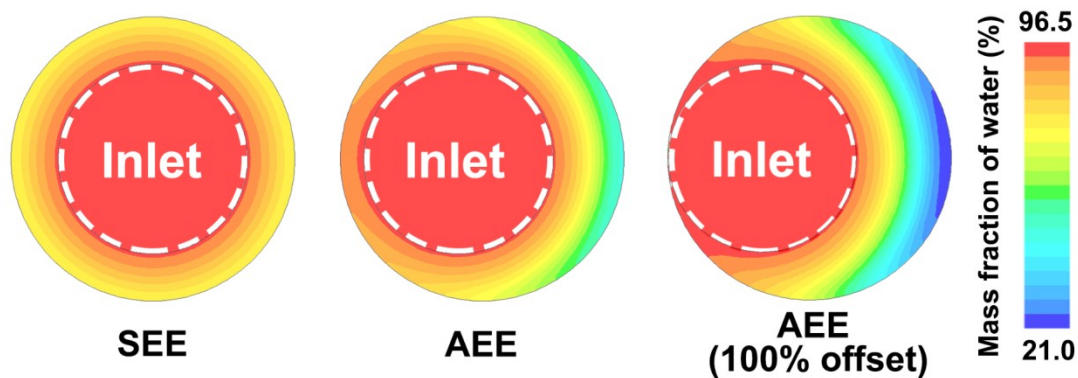
Fig. S11. Water content (mass fraction) profiles of PAM-CBF discs in SEE, AEE, and AEE (100% offset) under one-sun irradiation predicted by CFD simulation.

The increased presence of green and blue areas in the AEE and AEE (100% offset) indicates that the water layer on these surfaces is thinner compared to that on SEE. Consequently, AEE and AEE (100% offset) utilize the same amount of energy (equivalent light area and intensity) to heat a reduced volume of water relative to SEE. **When surface salt coverage is not considered, this leads to higher evaporation rates for AEE and AEE (100%).**
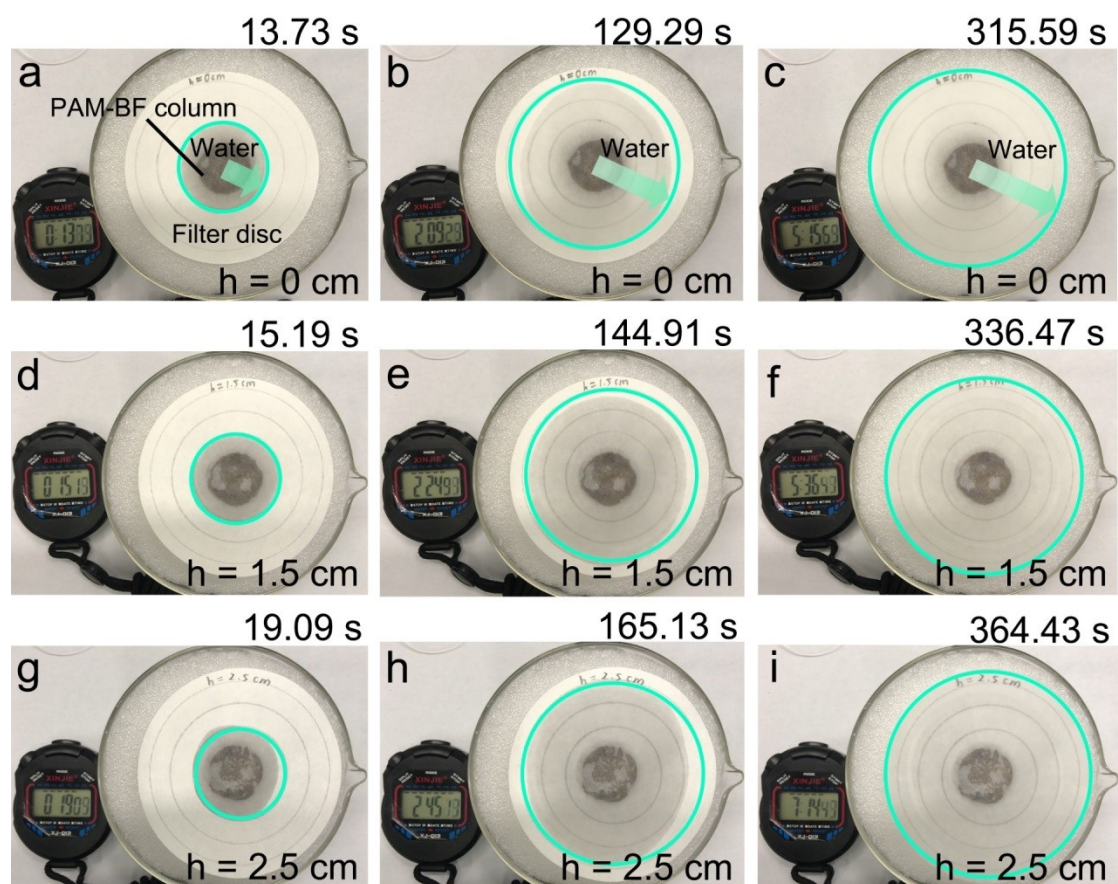
Fig. S12. Comparison of water delivery ability of the PAM-BF column with different heights beyond the EPE foam: (a-c) 0 cm; (d-f) 1.5 cm; (g-i) 2.5 cm.

This experiment aimed to investigate the relationship between the height of the PAM-BF column extending beyond the EPE foam and its rate of water transportation. The experimental setup consisted of a water storage container, a EPE foam, a PAM-BF column, and a filter paper disc, similar to the configuration of the SEE and AEE. Our observations revealed that elevating the height of the PAM-BF column above the EPE foam resulted in a decrease in the rate of water diffusion on the filter paper disc placed above it. **These findings indicate that as the height of the column beyond the EPE foam increases, its water transportation capacity reduces.** Furthermore, it was noticed that water diffusion towards the perimeter of the filter paper disc was initially rapid but gradually decelerated.
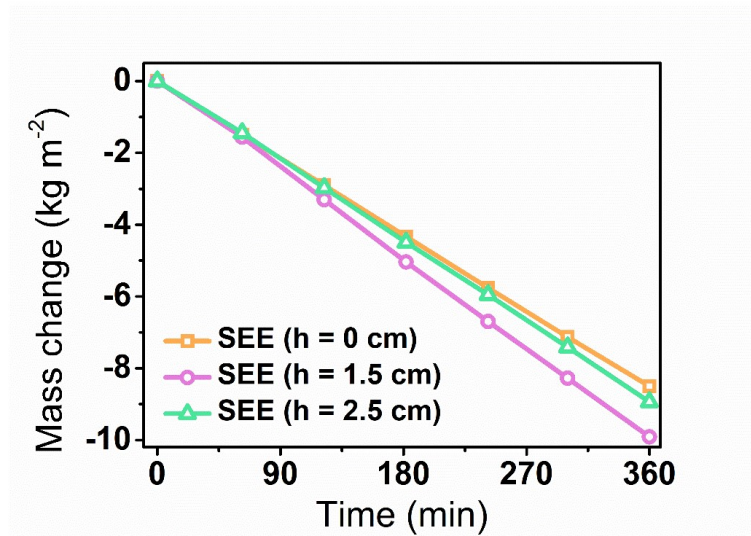
Fig. S13. Comparison of seawater mass change curves of SEE with different PAM-BF column heights (0 cm, 1.5 cm, and 2.5 cm beyond EPE foam) under one-sun irradiation.

The results indicate that the highest rate of water evaporation was observed when the PAM-BF column extended 1.5 cm beyond the EPE foam. This enhanced evaporation can be attributed to the optimal balance between water transport and evaporation rates.[32] **Based on these findings, a PAM-BF column height of 1.5 cm outside the EPE foam is recommended to achieve optimal evaporation performance.**
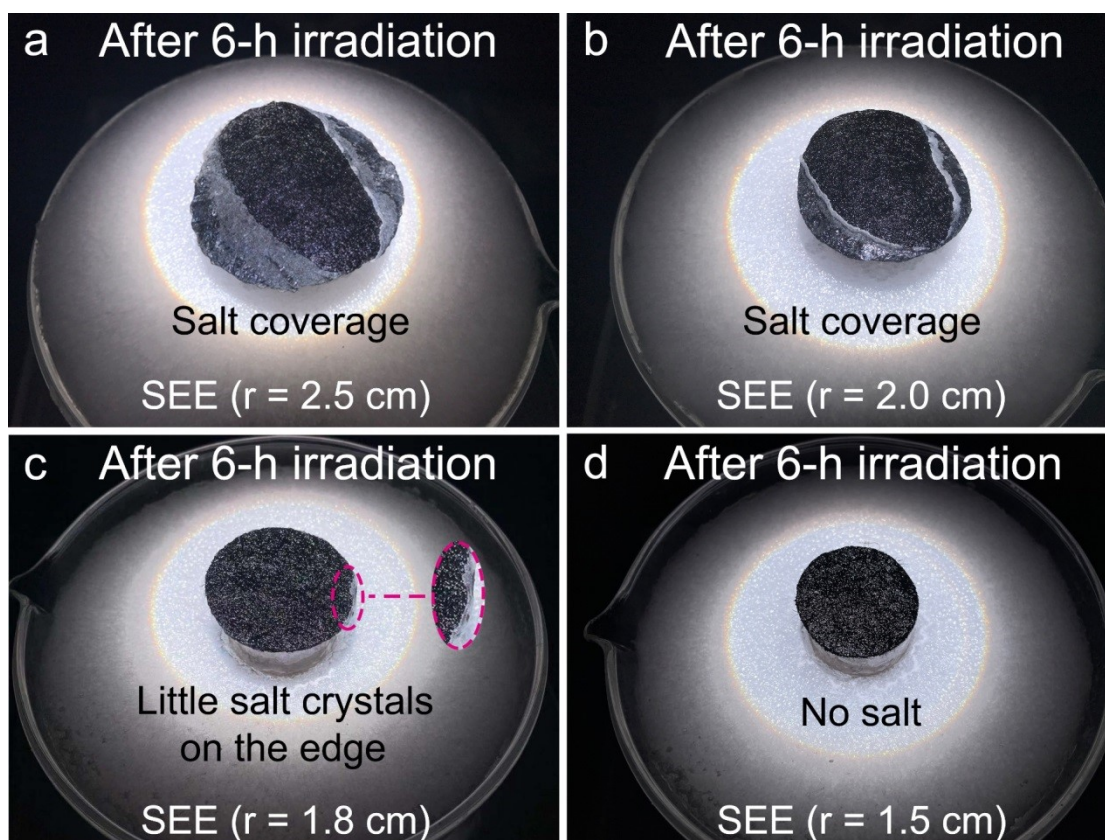
Fig. S14. Salt accumulation on SEE with different radii during evaporation: (a) r = 2.5 cm; (b) r = 2.0 cm; (c) r = 1.8 cm; (d) r = 1.5 cm.

When the radius of SEE is set to 2.5 cm or 2.0 cm, the salt produced covers the evaporation surface, resulting in reduced operational efficiency and stability. Conversely, when the radius is 1.5 cm, no salt crystals form on the surface or edges of the SEE due to the high-speed water transport capacity at the center. However, this absence of salt crystal formation is not conducive to effective salt extraction. **Notably, when the radius is adjusted to 1.8 cm, the solid salt tends to concentrate and precipitate at the edge of the SEE, without obstructing the evaporation surface. Thus, based on these findings, a radius of 1.8 cm was determined to be the optimal size for the PAM-CBF disc.**
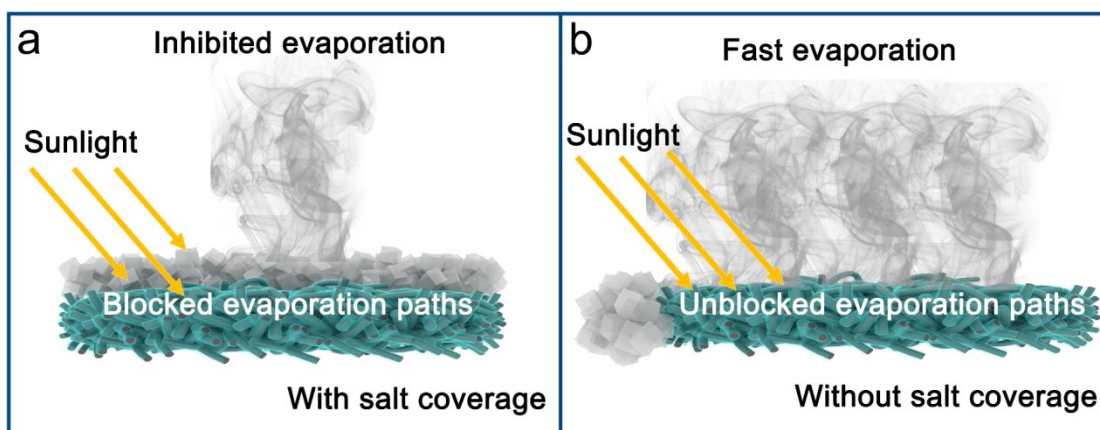
Fig. S15. Schematic illustration of the effect of different forms of salt accumulation on light absorption and vapor escape from the surface of the evaporator: (a) salt accumulation on the surface; (b) salt accumulation at the edge.

The presence of solid salt covering the evaporation surface obstructs incident light and prevents the escape of water vapor. **To ensure efficient operation of the evaporator and effective utilization of salt resources, it is necessary to promote the formation of solid salt at the edge of the evaporator.** PAM-CBF discs with radii of 2.5 cm and 2.0 cm cannot fulfill this requirement. When the radius was set to 1.5 cm, solid salt could not be precipitated. Therefore, **the optimal radius of the PAM-CBF was determined to be 1.8 cm, striking a balance between efficient evaporation and salt resource utilization.**
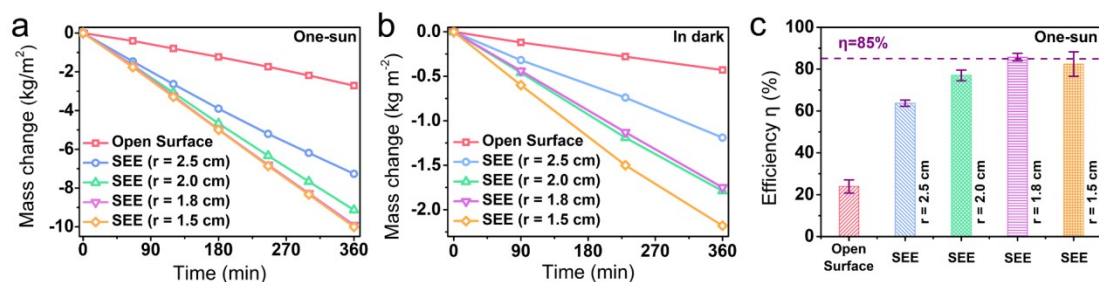
Fig. S16. Water evaporation performance of SEEs with different radii. Comparison of seawater mass change of open surface and SEEs with different radii (a) under one-sun irradiation and (b) in dark. (c) Comparison of solar-to-vapor efficiency of the open surface and SEEs with different radii under one-sun irradiation.

Excessively large evaporation surfaces may impede adequate air convection across the evaporator surface, resulting in a central zone with high humidity and compromised evaporation performance.[33] Consequently, when the radius of SEE exceeds 1.8 cm, its evaporation performance under light conditions diminishes as the radius increases. Conversely, when the radius is less than or equal to 1.8 cm, the evaporation rate trends to stabilize. In terms of solar-to-vapor efficiency, the **SEE with a radius of 1.8 cm demonstrates optimal evaporation performance. Moreover, the PAM-CBF disc radius was optimized to 1.8 cm, considering the need for efficient evaporation and salt collection.**
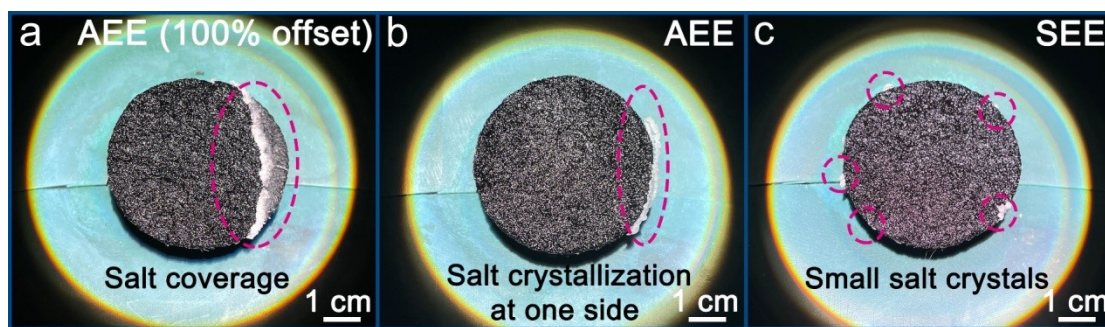
Fig. S17. Images of salt accumulation during evaporation: (a) AEE (100% offset); (b) AEE; (c) SEE.

In the SEE, AEE, and AEE (100% offset), solid salt is observed to scatter randomly at the edges of the SEE, posing challenges for efficient collection. Additionally, the precipitated solid salt partially covers the evaporation surface of the AEE (100% offset), reducing its performance and complicating automated salt collection. In contrast, **only the use of AEE ensures the concentration of a substantial amount of solid salt at one edge of the evaporator, thereby facilitating efficient evaporation and convenient salt collection**.
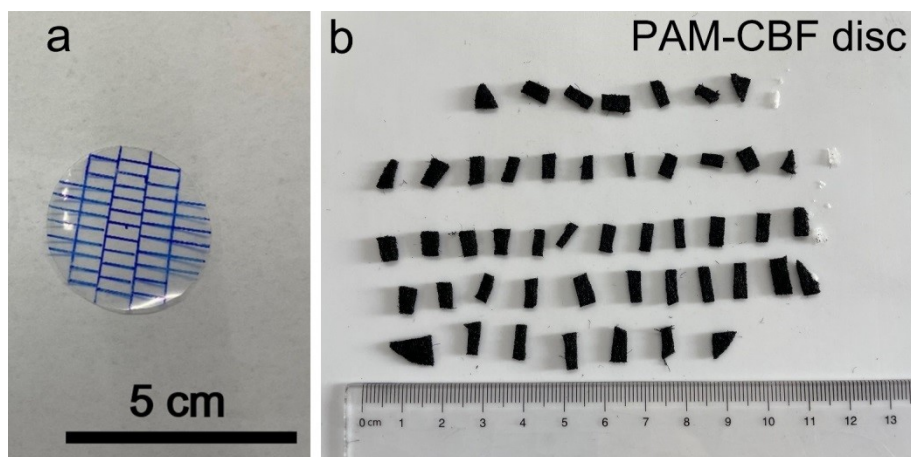
Fig. S18. (a) Diagram of the design of the cut for the PAM-CBF disc. (b) Fragments formed by cutting the PAM-CBF disc.

After 10 hours of exposure to one-sun irradiation, the PAM-CBF disc on the AEE was carefully removed and dismantled into small fragments by following the design drawing. The resulting smaller fragments were carefully labelled, and the area of each fragment was precisely measured using specialized software (ImageJ). Subsequently, each small fragment was immersed in a fixed volume (12 mL) of deionized water to facilitate the extraction of salt. By visualizing the actual salt concentration, the salt content in these fragments could be accurately determined.
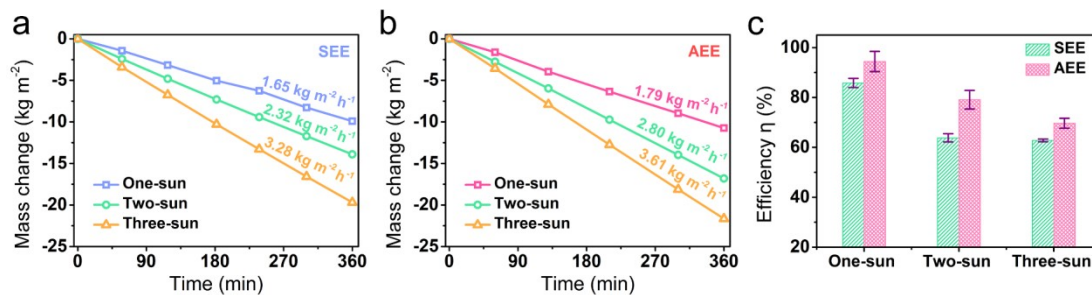
Fig. S19. Evaporation performance of SEE and AEE under different irradiation conditions. Seawater mass change of (a) SEE and (b) AEE under different irradiation intensities. (c) Comparison of solar-to-vapor efficiency between SEE and AEE under different irradiation intensities.

The comparative analysis of evaporation rates and solar-to-vapor efficiencies reveal that AEE outperforms SEE across various irradiation intensities, highlighting the superior solar evaporation characteristics of AEE.
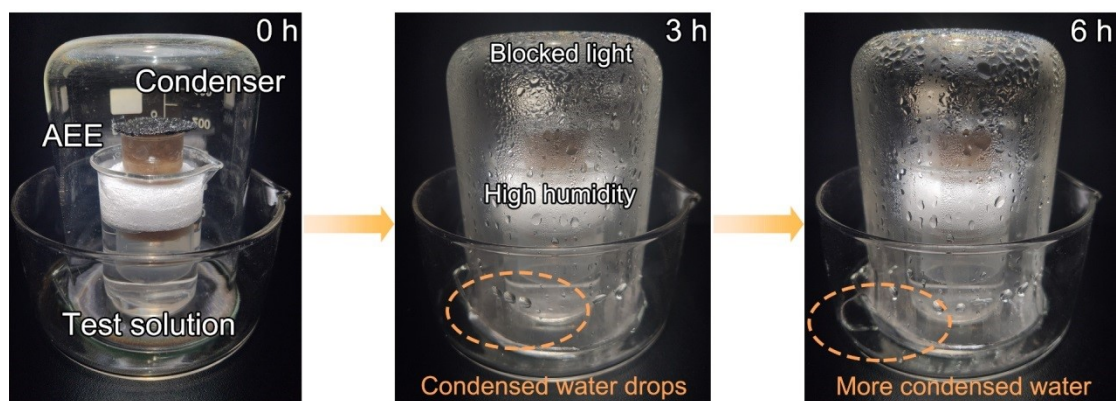
Fig. S20. Custom-built water treatment device employing AEE for seawater desalination testing.

The custom-built water treatment device consists of a condenser, a vessel containing simulated seawater, and an AEE. After 3 hours of irradiation, numerous condensation droplets were observed on the inner wall of the condenser. The amount of condensation freshwater further increased after 6 hours of irradiation. Throughout the 6-hour test, 5.80 g of water evaporated from the simulated seawater, and 4.72 g of condensate was collected. As a result, the recovery rate of freshwater extraction from this simple device is 81.38% over 6 hours.
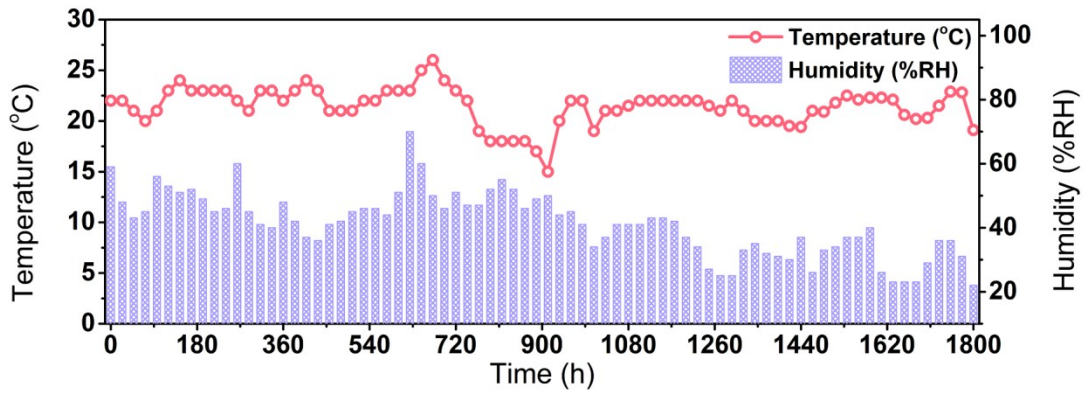
Fig. S21. Temperature and humidity variations during the 1800-hour evaporation test.

During the 1800-hour test, there were fluctuations in both ambient temperature and humidity levels. Periods of high humidity, exceeding 60%, were primarily caused by rainfall, while low humidity levels below 40% occurred during consecutive sunny days. Additionally, temperature fluctuations were also influenced by changes in the weather conditions.
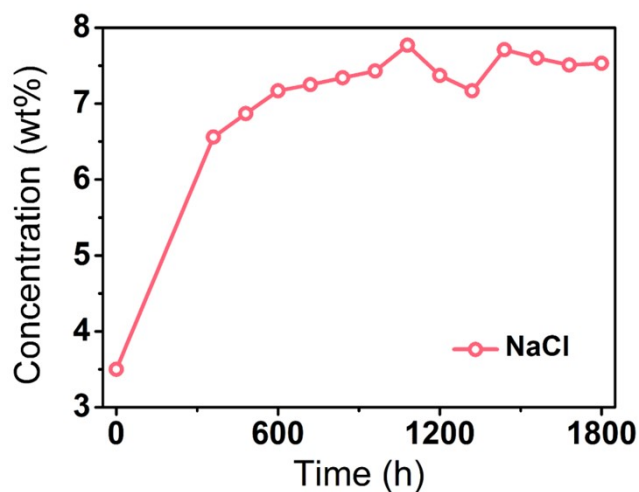
Fig. S22. Seawater concentration variations during the 1800-hour evaporation test.

Due to the fixed size of the container holding the simulated seawater, the available amount of seawater as a supply would have gradually decreased without replenishment during the 1800-hour continuous water evaporation and salt collection testing. To mimic a real seawater evaporation scenario with an unlimited supply, the simulated seawater was replenished daily to maintain a consistent level in the container. Initially, the concentration of the simulated seawater increased and then stabilized over the course of the test. This stability can be attributed to the equilibrium established between water evaporation, salt precipitation, and seawater replenishment.

Fig. S23. An indoor scaled-up evaporation device constructed by 4 AEEs.

The scaled-up device, which includes 4 AEEs, retains the ability for asymmetric salt precipitation in each AEE's designated area during testing. In addition, the accumulated salt consistently lands within a predetermined area, facilitating streamlined collection efforts. The outcomes highlight the scalability of AEEs.

Fig. S24. Outdoor evaporation test system.

The outdoor evaporation test system is made up of an evaporation device, built with 4 AEEs and a seawater container, a windscreen to minimize natural wind effects, an electronic balance for measuring the device's real-time weight, a light irradiation meter for measuring sunlight intensity in real-time, and a laptop that records the weights from the electronic balance.
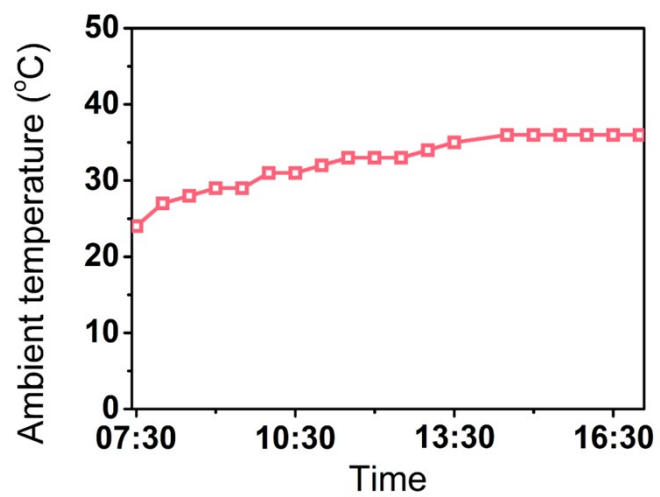
Fig. S25. Fluctuations in ambient temperature during the outdoor evaporation test.
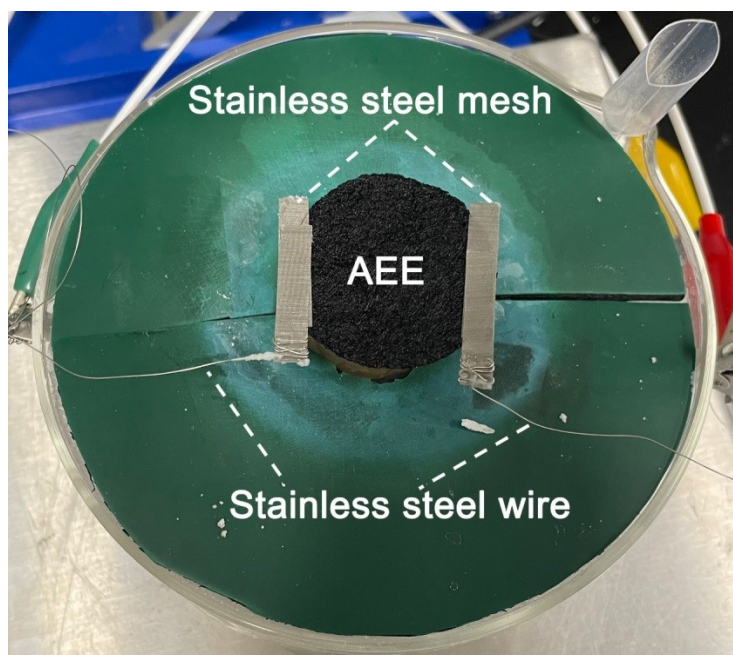
Fig. S26. Custom-built AEE-based device for extracting electrical energy.

In the custom-built device designed to extract electrical energy using AEE, 2 stainless steel mesh electrodes were securely fastened on either side of the PAM-CBF disc. These electrodes were connected to the electrochemical workstation by stainless steel wires, facilitating voltage and current measurements.
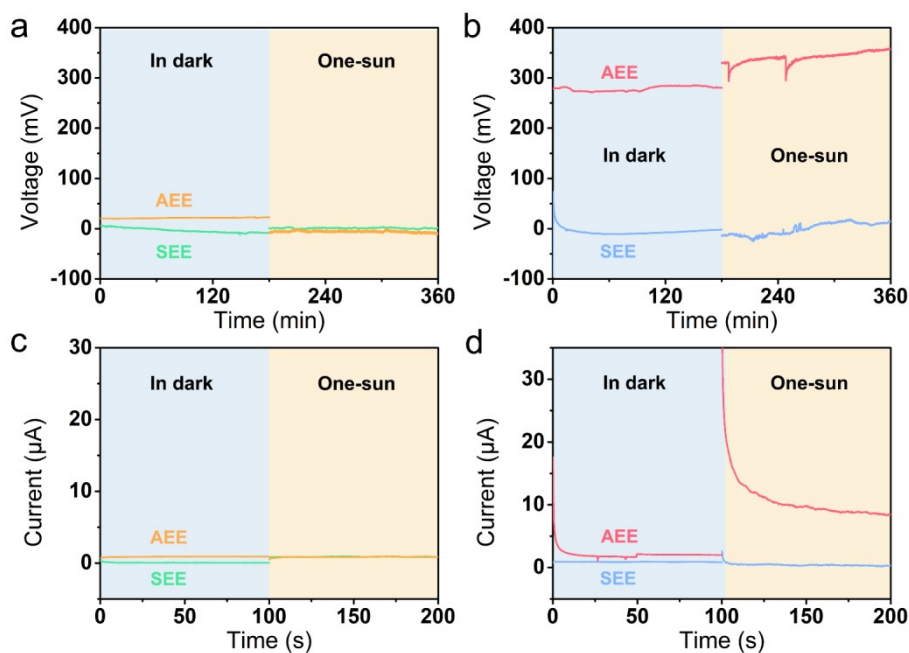
Fig. S27. Comparison of the performance of electricity extraction using SEE- and AEE-based devices under different conditions. (a) Voltage profiles for SEE- and AEE-based devices utilizing deionized water in both dark and irradiated conditions. (b) Voltage profiles for devices using seawater, contrasting their performance in darkness versus under irradiation. (c) Current profiles for devices with deionized water, comparing dark and irradiated environments. (d) Current profiles for devices using seawater under varying lighting conditions, evaluating their performance in darkness and when irradiated.

In deionized water, both AEE and SEE-based devices do not yield significant electrical signals in terms of voltage and current (Fig. S27a and c). Moreover, the performance of SEE-based devices in seawater is akin to their performance in deionized water, where no electrical signals are generated. In contrast, only the AEE-based device can produce voltages and currents in seawater, irrespective of exposure to dark or light conditions (Fig. S27b and d). **Thus, the asymmetric evaporation pattern and the presence of inorganic salts in the water are pivotal factors in**

driving the electrical output. Additionally, there is an initial current drop in the current versus time curve of the AEE-based device output, which is caused by the rapid formation of internal resistance in the circuit after connecting the test circuit.[34] Subsequently, once the internal resistance has stabilized, the current stabilizes as well. It should be noted that the light intensity used in this experiment was equivalent to one-sun irradiation.
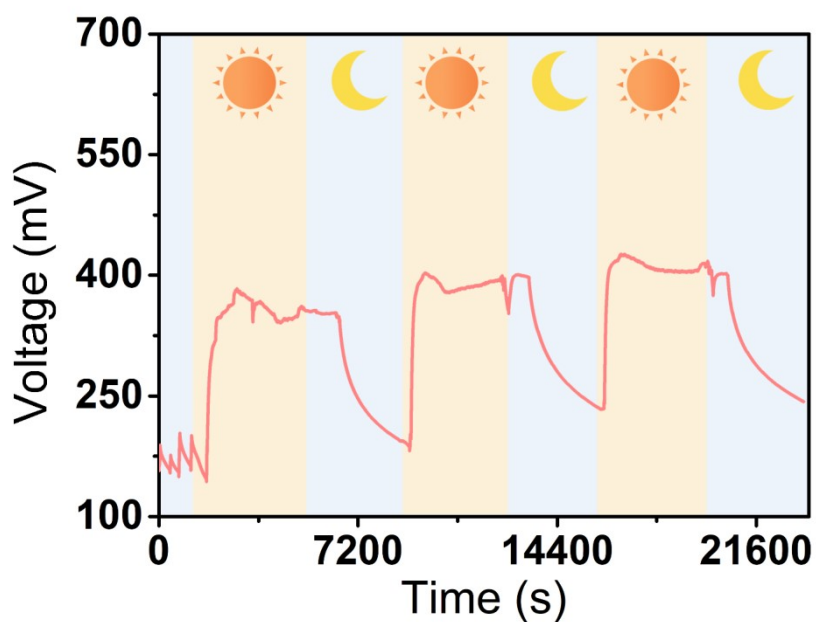
Fig. S28. The influence of light-dark cycles on the voltage output of AEE.

The stainless steel electrode partially obstructs light, which could potentially compromise efficiency and testing stability in the long run. To enhance the long-term stability of our experiments, the stainless steel mesh was substituted with carbon fiber filaments as electrodes in this electrical energy generation test utilizing the AEE. These filaments provide less obstruction to light. Nevertheless, this adjustment has modified the electrode's connection uniformity to the evaporation surface, causing some discrepancies in the steady voltage output of the AEE when carbon fiber filaments are compared to the stainless steel mesh.
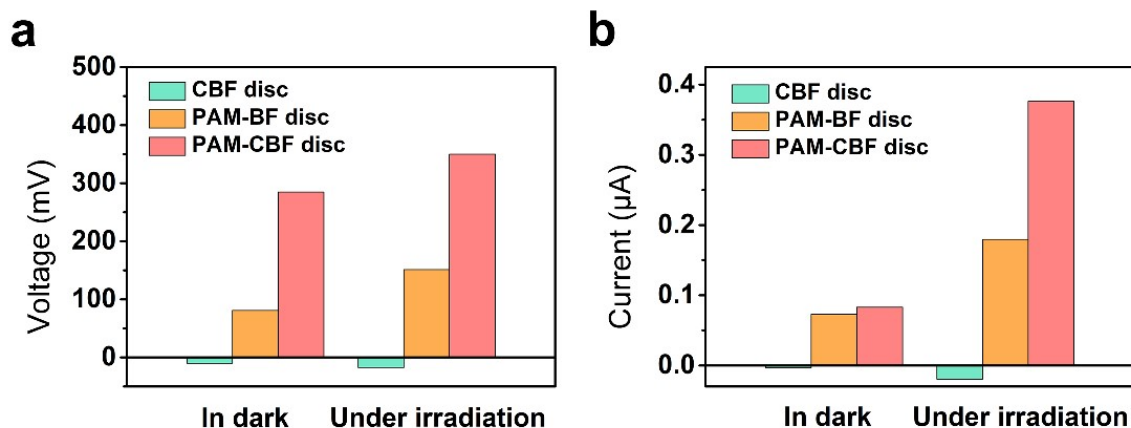
Fig. S29. (a) Voltage output and (b) current output of AEEs based on CBF disc, PAM-BF disc, and PAM-CBF disc in dark and under irradiation.

During the preparation of PAM-CBF disc and PAM-BF disc, the amount of PAM gel precursor was kept consistent for comparison. The low-temperature carbonization process from BF disc to CBF disc results in volumetric shrinkage. Consequently, when using the same amount of PAM gel, the PAM-CBF disc has a smaller volume compared to the PAM-BF disc, leading to a higher concentration of PAM gel per unit volume. This, in turn, enhances the electrical energy generation performance of the AEE equipped with the PAM-CBF disc compared to the one made with the PAM-BF disc.

The stainless steel electrode partially obstructs light, which could potentially compromise efficiency and testing stability in the long run. To enhance the long-term stability of our experiments, the stainless steel mesh was substituted with carbon fiber filaments as electrodes in these electrical energy generation tests utilizing the AEE. These filaments provide less obstruction to light. Nevertheless, this adjustment has modified the electrode's connection uniformity to the evaporation surface, causing some discrepancies in the steady voltage output of the AEE when carbon fiber filaments are compared to the stainless steel mesh. Moreover, carbon fiber filaments have a considerably smaller contact area with the evaporation surface of the AEE in

comparison to the stainless steel mesh. Consequently, the output current of the AEE with carbon fiber filaments as electrodes is significantly lower than that of the AEE using stainless steel mesh electrodes.
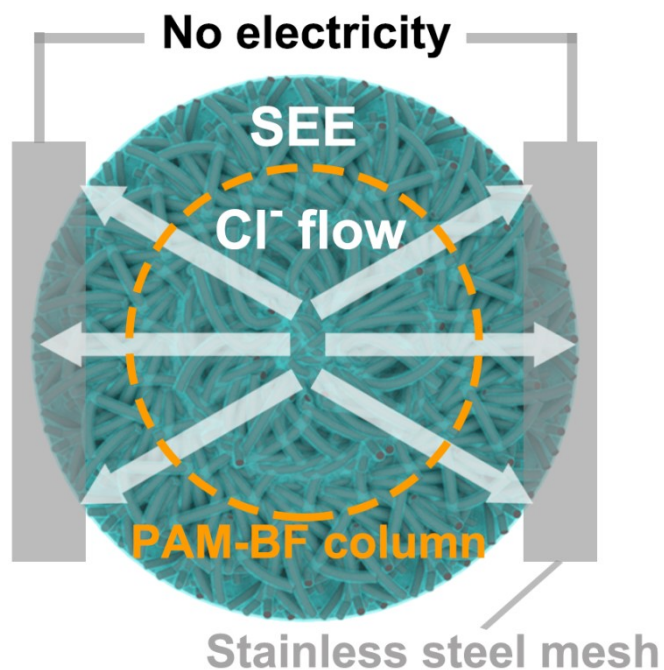
Fig. S30. Schematic of Cl⁻ ion flow in the PAM-CBF disc of SEE during evaporation.

In the SEE, all edges of the PAM-CBF disc are relatively equidistant from the seawater supply center. As a result, no significant difference in Cl⁻ ion concentration can be formed between these edges, thus eliminating the ability to create a potential difference.
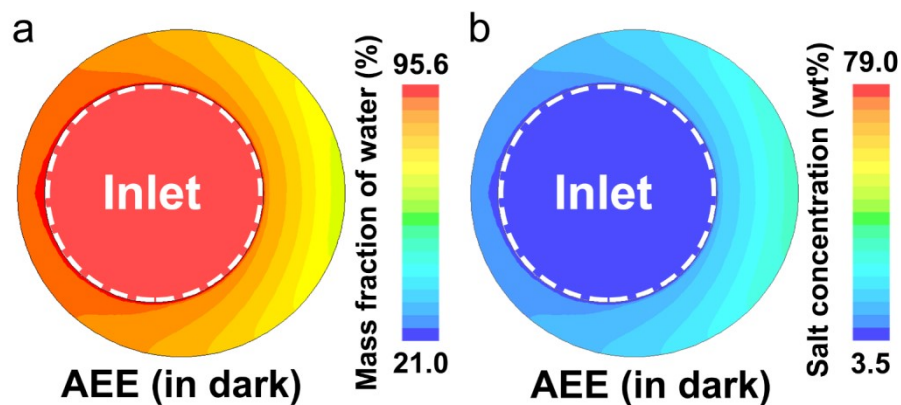
Fig. S31. Distribution characteristics of (a) water content and (b) salt concentration of PAM-CBF disc in AEE under dark condition predicted by CFD simulation.

In the absence of light, the evaporation rate of the AEE decreased significantly compared to that under irradiation, leading to a reduced gradient of both water content and salt concentration within the PAM-CBF disc of AEE.
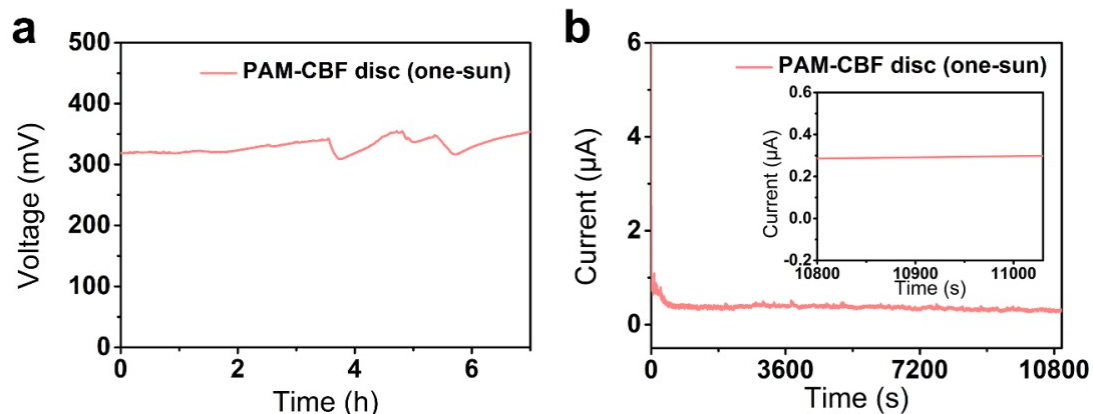
Fig. S32. The long-term tests of (a) voltage output and (b) current output of AEE based on PAM-CBF disc under one-sun irradiation.

The stainless steel electrode partially obstructs light, which could potentially compromise efficiency and testing stability in the long run. To enhance the long-term stability of our experiments, the stainless steel mesh was substituted with carbon fiber filaments as electrodes in this electrical energy generation test utilizing the AEE. These filaments provide less obstruction to light. Nevertheless, this adjustment has modified the electrode's connection uniformity to the evaporation surface, causing some discrepancies in the steady voltage output of the AEE when carbon fiber filaments are compared to the stainless steel mesh. Moreover, carbon fiber filaments have a considerably smaller contact area with the evaporation surface of the AEE in comparison to the stainless steel mesh. Consequently, the output current of the AEE with carbon fiber filaments as electrodes is significantly lower than that of the AEE using stainless steel mesh electrodes.

Fig. S33. (a) Schematic illustration and (b) photograph of an AEE-based device for the simultaneous extraction of freshwater, salt and electrical energy.

To demonstrate the ability of AEE to simultaneously produce freshwater, salt, and electrical energy simultaneously, we designed a device as shown in Fig. S33a. To minimize the effect of the electrodes on salt collection, the stainless steel mesh electrodes were replaced with carbon fiber electrodes that penetrate the PAM-CBF disc to collect electrical energy. The results indicate that the AEE-based device possesses the capability to simultaneously generate freshwater, salt, and electrical energy (Fig. S33b).

It is worth noting that the change in the connection method (drilling holes in the PAM-CBF disc and then threading in carbon fibers) resulted in a decrease in voltage output. This is due to the fact that, in order to prevent damage to the structure of PAM-CBF disc, the electrode connection position was forced closer to the center of the PAM-CBF disc compared to when the stainless steel mesh was used. This resulted in a reduction in the difference in Cl^- ion concentration between the two electrodes.

Supplementary References

1. H. Ghasemi, G. Ni, A. M. Marconnet, J. Loomis, S. Yerci, N. Miljkovic and G. Chen, *Nat. Commun.*, 2014, **5**, 4449.

2. Y. Xia, Q. Hou, H. Jubaer, Y. Li, Y. Kang, S. Yuan, H. Liu, M. W. Woo, L. Zhang, L. Gao, H. Wang and X. Zhang, *Energy Environ. Sci.*, 2019, **12**, 1840-1847.

3. J. Gao, J. Chen, H. Lv, X. Feng, S. Liao, L. Zhang, F. Ma, Y. Xue, M. Ji and H. Wang, *Sep. Purif. Technol.*, 2024, **329**, 125168.

4. G. Ni, S. H. Zandavi, S. M. Javid, S. V. Boriskina, T. A. Cooper and G. Chen, *Energy Environ. Sci.*, 2018, **11**, 1510-1519.

5. P. Xiao, J. Gu, C. Zhang, F. Ni, Y. Liang, J. He, L. Zhang, J. Ouyang, S.-W. Kuo and T. Chen, *Nano Energy*, 2019, **65**, 104002.

6. H. M. Wilson, S. Rahman A.R, A. E. Parab and N. Jha, *Desalination.*, 2019, **456**, 85-96.

7. L. Chen, H. Wang, S. Kuravi, K. Kota, Y. H. Park and P. Xu, *Desalination.*, 2020, **483**, 114412.

8. Y. Xu, B. Lv, Y. Yang, X. Fan, Y. Yu, C. Song and Y. Liu, *Desalination.*, 2021, **517**, 115260.

9. Y. Zhu, G. Tian, Y. Liu, H. Li, P. Zhang, L. Zhan, R. Gao and C. Huang, *Adv. Sci.*, 2021, **8**, 2101727.

10. M. Yin, Y. Hsin, X. Guo, R. Zhang, X. Huang and X. Zhang, *Sci. Total. Environ.*, 2021, **759**, 143546.

11. F. Liu, B. Zhao, W. Wu, H. Yang, Y. Ning, Y. Lai and R. Bradley, *Adv. Funct. Mater.*, 2018, **28**, 1803266.

12. H. Li, Y. He, Y. Hu and X. Wang, *ACS Appl. Mater. Interfaces*, 2018, **10**, 9362-9368.

13. Y. Guo, H. Lu, F. Zhao, X. Zhou, W. Shi and G. Yu, *Adv. Mater.*, 2020, **32**, 1907061.

14. J. Zeng, Q. Wang, Y. Shi, P. Liu and R. Chen, *Adv. Energy Mater.*, 2019, **9**, 1900552.

15. G. Chen, J. Sun, Q. Peng, Q. Sun, G. Wang, Y. Cai, X. Gu, Z. Shuai and B. Z. Tang, *Adv. Mater.*, 2020, **32**, 1908537.

16. L. Zhu, T. Ding, M. Gao, C. K. N. Peh and G. W. Ho, *Adv. Energy Mater.*, 2019, **9**, 1900250.

17. K. Li, T.-H. Chang, Z. Li, H. Yang, F. Fu, T. Li, J. S. Ho and P.-Y. Chen, *Adv. Energy Mater.*, 2019, **9**, 1901687.

18. Y. Zou, X. Chen, P. Yang, G. Liang, Y. Yang, Z. Gu and Y. Li, *Sci. Adv.*, 2020, **6**, eabb4696.

19. Q. Xia, Y. Pan, B. Liu, X. Zhang, E. Li, T. Shen, S. Li, N. Xu, J. Ding, C. Wang, C. D. Vecitis and G. Gao, *Sci. Adv.*, 2024, **10**, eadj3760.

20. M. Wang, Y. Wei, X. Wang, R. Li, S. Zhang, K. Wang, R. Wang, H. Chang, C. Wang, N. Ren and S.-H. Ho, *Nat. Water*, 2023, **1**, 716-724.

21. J. Mao, J.-J. Li, A.-Q. Xie, Y. Liang, Y. Yang, L. Zhu and S. Chen, *Sol. RRL*, 2022, **6**, 2200330.

22. J. Xu, Z. Wang, C. Chang, B. Fu, P. Tao, C. Song, W. Shang and T. Deng, *Desalination.*, 2020, **484**, 114423.

23. H. Peng, D. Wang and S. Fu, *Chem. Eng. J.*, 2021, **426**, 131818.

24. X. Ma, X. Wan, Z. Fang, Z. Li, X. Wang, Y. Hu, M. Dong, Z. Ye and X. Peng, *Desalination.*, 2022, **522**, 115399.

25. Z. Yang, D. Li, K. Yang, L. Chen, J. Wang, X. Zhu and B. Chen, *Environ. Sci. Technol.*, 2023, **57**, 13047-13055.

26. M. A. Abdelsalam, M. Sajjad, A. Raza, F. AlMarzooqi and T. Zhang, *Nat. Commun.*, 2024, **15**, 874.

27. X. Mu, J. Zhou, P. Wang, H. Chen, T. Yang, S. Chen, L. Miao and T. Mori, *Energy Environ. Sci.*, 2022, **15**, 3388-3399.

28. P. Yang, K. Liu, Q. Chen, J. Li, J. Duan, G. Xue, Z. Xu, W. Xie and J. Zhou, *Energy Environ. Sci.*, 2017, **10**, 1923-1927.

29. Z. Sun, C. Han, S. Gao, Z. Li, M. Jing, H. Yu and Z. Wang, *Nat. Commun.*, 2022, **13**, 5077.

30. Y. Xu, J. Xu, J. Zhang, X. Li, B. Fu, C. Song, W. Shang, P. Tao and T. Deng, *Nano Energy*, 2022, **93**, 106882.

31. Q. Hu, X. Lin, G. Ren, J. Lü, W. Wang, D. Zhang and S. Zhou, *Nat. Water*, 2024, DOI: 10.1038/s44221-024-00311-9.

32. Y. Li, W. Hong, H. Li, Z. Yan, S. Wang, X. Liu, B. Li, H. Jiang and X. Niu, *Desalination.*, 2021, **511**, 115113.

33. T. Gao, Y. Wang, X. Wu, P. Wu, X. Yang, Q. Li, Z. Zhang, D. Zhang, G. Owens and H. Xu, *Sci. Bull.*, 2022, **67**, 1572-1580.

34. Y. Shao, M. F. El-Kady, J. Sun, Y. Li, Q. Zhang, M. Zhu, H. Wang, B. Dunn and R. B. Kaner, *Chem. Rev.*, 2018, **118**, 9233-9280.